Check for updates

View Article Online
View Journal

Journal of
Materials Chemistry A

Materials for energy and sustainability

Accepted Manuscript

This article can be cited before page numbers have been issued, to do this please use: R. R. Koli, Y. Tsai, Y. Huang, C. Wang, B. Liu, P. Raghunath, M. C. Lin and E. W. Diau, *J. Mater. Chem. A*, 2025, DOI: 10.1039/D5TA03793J.

This is an Accepted Manuscript, which has been through the Royal Society of Chemistry peer review process and has been accepted for publication.

Accepted Manuscripts are published online shortly after acceptance, before technical editing, formatting and proof reading. Using this free service, authors can make their results available to the community, in citable form, before we publish the edited article. We will replace this Accepted Manuscript with the edited and formatted Advance Article as soon as it is available.

You can find more information about Accepted Manuscripts in the Information for Authors.

Please note that technical editing may introduce minor changes to the text and/or graphics, which may alter content. The journal's standard Terms & Conditions and the Ethical guidelines still apply. In no event shall the Royal Society of Chemistry be held responsible for any errors or omissions in this Accepted Manuscript or any consequences arising from the use of any information it contains.

ROYAL SOCIETY OF CHEMISTRY

rsc.li/materials-a

View Article Online
DOI: 10.1039/D5TA03793J

ARTICLE

Development of Single Crystalline Al-doped ZnS Nanodiscs as Efficient Photocatalysts for H_2 Evolution Reaction†

Received 00th January 20xx,
Accepted 00th January 20xx

DOI: 10.1039/x0xx00000x

Rohit R. Koli[a], I-Hua Tsai[a], Yu-Bin Huang[b], Chia-Hsin Wang[b], Bo-Hong Liu[b], Raghunath Putikam[a], M. C. Lin[a], Eric Wei-Guang Diau[a, c]*

The rapid photoinduced charge carrier recombination hinders the photocatalytic efficiency of binary zinc sulfide (ZS) photocatalysts. Enhanced charge separation by the electronic and band structure modification via metal cation doping has gained much attention. Herein, aluminum (Al) doping with Pt single atom (SA) into single crystalline ZnS nanodiscs (Pt-AZS) with shallow defect states is reported. The Rietveld refinement of XRD confirms lattice expansion with modulated electronic distribution. The additional Al-electron traps improved the lifetime of charge carriers to enhance their interfacial transport to the metal cocatalyst, which is confirmed by in-situ XPS and time-resolved photoluminescence spectroscopy. The 1.6 wt.% Pt loading on the AZS (200) facet exhibits an enhanced H_2 evolution rate of 17.1 mmol g^{-1} h^{-1} under AM1.5G irradiation with an apparent quantum yield (AQY) of 34% at 345 nm using a WB40 filter. Under UV light irradiation, Pt-AZS showed a great H_2 generation rate of 38 mmol g^{-1} h^{-1}, which is two times more than the bare Pt-ZS. This work elucidates the efficacy of Al doping with Pt SA in a single crystalline photocatalyst to facilitate electron transport via suppressed band-bending at the Mott-Schottky interface, intended to boost up the photocatalytic H_2 production.

1. Introduction

Rapid industrialization is causing energy crises and environmental pollution challenges. Finding an alternate eco-friendly energy source is crucial for the long-term growth of human civilization. Regarding this, hydrogen (H_2) is a promising fossil fuel replacement owing to its renewable, carbon-neutral, energy-dense, and compressible nature for uninterrupted transportation.[1–3] However, the current rise of energy demand, poor efficiency, and ecologically harmful H_2 generation technologies limit the commercial use of hydrogen energy.[4,5] Alternatively, photo-induced water splitting can efficiently convert solar energy to chemical energy (H_2) without polluting, making it a viable and sustainable approach.[6,7]

Among inorganic photocatalysts, metal chalcogenides, including CdS, Cu_7S_4, $CdIn_2S_4$, and $ZnIn_2S_4$ (ZIS), have garnered interest for their excellent visible/IR-light response.[8–11] The photocatalytic property of most of these chalcogenides is unsatisfactory due to their fast carrier recombination and structural instability by photocorrosion in full sunlight irradiation. In this regard, ZnS is a low-toxic, UV-stable alternative with a high conduction band (CB) level beneficial for photoreduction of water to H_2 (H_2 evolution reaction, HER) without any co-catalyst.[12,13] To enhance its performance, researchers have made significant efforts in band engineering of pristine ZnS using metal cation doping, heterojunction, and surface modification by metal single atoms (SAs).[14–19] Among these, co-doping ZnS with Al/Ga/In and Cu resulted in a moderate enhancement in its photocatalytic activity.[20–23] chalcogenides, the anion vacancies have seemed to create defect states, which benefit electron trapping for accelerated photocarrier separation.[24,25] Nevertheless, more trap states may also serve as photocarrier recombination sites, reducing photocatalytic efficacy, which can be avoided by ensuring proper defect concentration.[26] In the case of ZnS, along with S (anion) vacancies, modification in electronic structure of photocatalysts by SA doping of metal cations can be an effective strategy for tuning band edge position and controlled formation of donor/acceptor impurity levels.[27] Accordingly, in-situ non-noble metal substitution at Zn sites was investigated to reduce intermediate recombination sites and to improve the photocatalytic performance of ZnS.

Previous studies have investigated H_2 production using ZnS doped with Cu, Ni, and Pb cations. The Cu-doped ZnS has shown a shallow Cu^{2+} donor level and demonstrated a high apparent quantum yield (AQY) of 3.7%, while Ni-doped ZnS showed an AQY of 1.3% at 420 nm.[28] Despite having lower H_2 yield than the Cu-doped ZnS (yield ~6.25 mmol g^{-1} h^{-1}), Ni-doped ZnS (yield ~430 µmol g^{-1} h^{-1}) remained thermally and chemically stable. The best H_2 generation rate of 12 mmol g^{-1} h^{-1} with AQY of 12.67% was reported for Cu SA doped ZnS with Na_2S and Na_2SO_3 as hole scavengers.[26] However, Cu-doped ZnS suffers from photocorrosion, which can be resolved by co-doping of metal cations like Ga^{3+}, In^{3+} or Al^{3+} with Cu-doped ZnS[29] or surface

[a] Department of Applied Chemistry, National Yang Ming Chiao Tung University, Hsinchu 300093, Taiwan.
[b] National Synchrotron Radiation Research Center, Hsinchu 30076, Taiwan.
[c] Center for Emergent Functional Matter Science, National Yang Ming Chiao Tung University, Hsinchu 300093, Taiwan.

† Supplementary Information available: [experimental details, supplementary figures and tables would be included]. See DOI: 10.1039/x0xx00000x

Published on 28 August 2025. Downloaded by National Yang Ming Chiao Tung University on 9/8/2025 8:16:04 AM.

Journal of Materials Chemistry A Accepted Manuscript

View Article Online
DOI: 10.1039/D5TA03793J

Published on 28 August 2025. Downloaded by National Yang Ming Chiao Tung University on 9/8/2025 8:16:04 AM.

Journal of Materials Chemistry A Accepted Manuscript

modification by SA/NPs of noble metals like Au, Pt, and so on.[30] The reported maximum H_2 yield for such co-doped ZnS was below 4 mmol g^{-1} h^{-1}. [31] The anion vacancies seemed to be beneficial for introducing intermediate electron "traps" by the addition of mid-gap states. Recently, Shi et al. reported the highest H_2 yield of 17.5 mmol g^{-1} h^{-1} under visible light for Pt-decorated S-vacant ZIS (Pt-ZIS) with plenty of H_2 bubbles. However, the high cost and scarcity of In precursor is an obstacle for the practical use of ZIS in green H_2 production while, only S vacancies in ZnS were inefficient for significantly tuning its Fermi level and band positions. Previously, different metal-doped ZnS, including Al-doped ZnS polycrystalline structures, were studied for H_2 evolution with moderate improvement in H_2 yield.[20,32–37] The lack of favorable facet growth (particularly, having S-rich planes) can be the reason for inferior photocatalytic performance. Recently, Al-doped $SrTiO_3$ single crystalline sub-microparticles decorated by Rh/Cr_2O_3 nanoparticles showed quantum efficiency of almost unity for water splitting in the UV region.[38] Jia et al. showed the importance of directed charge transport in ferroelectric $Bi_4Ti_3O_{12}$ single crystal for overall water splitting under visible light irradiation.[39]

In the present study, enhanced photocatalytic HER performance using co-cationic doping in ZnS nanodiscs (NDs) is reported. A less reactive Al^{3+} cation was chosen as a dopant to avoid secondary phase formation and to ensure single crystalline growth along the (111) plane of the ZnS NDs for which the Al^{3+} cations occupy Zn^{2+} sites and the S-rich (200) plane directed the ZnS growth. A high H_2 evolution rate of 17.1 mmol g^{-1} h^{-1} with AQY of 34 % at 345 nm was achieved by Pt SAs anchored to Al-doped ZnS (Pt-AZS) NDs. The HER rate is comparable to that of the Pt-ZIS system, and it is also 30% higher than the previous record of the Cu-doped ZnS system[26]. In the photochemical reaction chamber with both UV-A and UV-B irradiations, the Pt-AZS photocatalyst attained a remarkable HER yield of 38 mmol g^{-1} h^{-1}, which is almost two times greater than that of the Pt-ZnS photocatalyst without Al-doping.

2. Experimental

2.1. Preparation of ZnS microdiscs by hydrothermal method

ZnS chalcogenide microdiscs (MDs) were synthesized by a moderately high-temperature hydrothermal method. The synthesis of ZnS MDs was done by dissolving 2.5 mmol of zinc acetate (Zn $(CH_3CO_2)_2{\cdot}2H_2O$) and 80 mmol of thioacetamide (C_2H_5NS) in 25 mL of deionized (DI) water separately to obtain colorless solutions. These zinc acetate (ZnAc) and thioacetamide (TAA) solutions were thoroughly mixed for 15 min under magnetic stirring and transferred to a 120 mL Teflon-lined autoclave. The final mixture volume was increased to 100 mL by the further addition of DI water. Then this Teflon lined autoclave was kept in a muffle furnace pre-programmed for 180 °C with an initial temperature rise of 12 °C/min, followed by 180 °C for 12h. After natural cooling, the product was washed with DI water and ethanol three times and dried in a vacuum oven at 60 °C overnight. The dried sample was ground in a mortar and pestle and denoted as ZS0 for further study.

2.2. Preparation of ZnS and AlSA- ZnS nanodiscs by the hydrothermal method

The synthesis of ZnS nanodiscs (NDs) was done by using a mixture of 2.5 mmol of ZnAc, 80 mmol of TAA, and 10 mmol of trisodium citrate dihydrate ($C_6H_5Na_3O_7{\cdot}2H_2O$), i.e., NaCt, in DI water. This mixture was then hydrothermally treated at 180° C in a Teflon-lined SS autoclave for 12 h. After cleaning and vacuum drying, the sample was abbreviated as ZS. In a similar way, Al-ZnS was hydrothermally synthesized by dissolving 2.5 mmol of ZnAc, 80 mmol of TAA, 10 mmol of NaCt and 5 mmol of anhydrous $AlCl_3$ in 25 mL of DI water separately. These solutions are then added to a 120 mL Teflon liner under magnetic stirring. The remaining cleaning process is similar to ZS. The vacuum-dried Al-doped fine powder sample was denoted by AZS.

3. Results and Discussion

3.1. Crystal growth and structure analysis

The hydrothermal synthetic procedures of ZS and AZS photocatalysts with ND shape and thickness below 50 nm are schematically shown in **Fig. 1**. The introduction of a reducing agent along with Al^{3+} cations (Zn:Al = 1:1) significantly lowers the nanoparticle size to 105 nm (Fig. S3c).

In AZS, the presence of two metal cations created S vacancies and as the formation energy of the compound for Al-substituted Zn sites is found to be minimum, Al preferably occupies some of these Zn positions.[40] To confirm the least formation energy of Al substitution and modification in electronic structure by lattice distortion, we performed the possible ways of introducing an Al atom into the ZnS (zinc blende) $\bar{F}43m$ structure, where the formation energies are computed using DFT calculations by implementing Vienna ab initio simulation package (VASP).[41] The 1.6 wt% Pt SAs were photodeposited on AZS by injecting aqueous H_2PtCl_6 (50 mg mL^{-1}) into aqueous dispersion of 2.5 mg AZS under AM 1.5G simulated light illumination.

Spherical aberration-corrected scanning transmission electron microscopy (Cs-corrected STEM) measurements were conducted on AZS and Pt-AZS to determine sample morphology and the configuration of the Pt co-catalyst (**Fig. 2**).

The optimized NaCt-assisted AZS sample had a uniform ND morphology with a diameter of 105 nm (Fig. 2a). The EDS line scan profiles measured at the middle position (in bulk) and at the edge of a single AZS nanoparticle differ in their elemental distribution (Figs. 2b and 2c). The uniform distribution of Zn and S in the EDS line scan measured at the middle (position 1) while the gradual reduction in net counts measured at the corner (position 2), confirms the ND morphology of AZS. Such a nanodisc surface can benefit from the preferential growth of Pt SA sites. The corresponding positions are shown in a high-angle annular dark field (HAADF) STEM image of AZS (Fig. 2d). The high-resolution TEM (HRTEM) image in Fig. 2e and atomic

This journal is © The Royal Society of Chemistry 20xx

Please do not adjust margins

View Article Online
DOI: 10.1039/D5TA03793J

Published on 28 August 2025. Downloaded by National Yang Ming Chiao Tung University on 9/8/2025 8:16:04 AM.

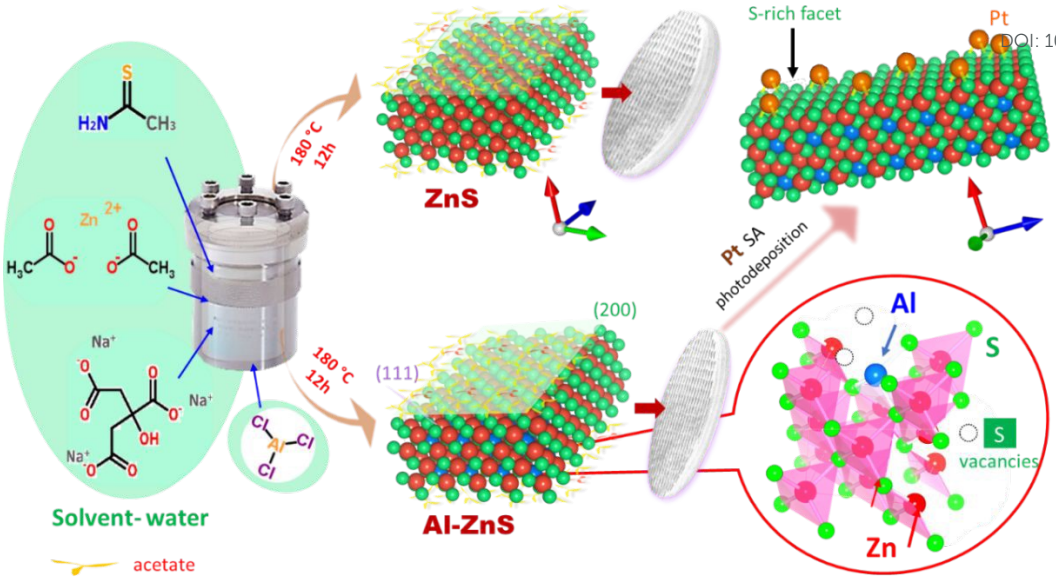

Fig. 1 Schematic presentation of hydrothermal synthesis of ZnS (ZS) and Al-ZnS (AZS) nanodiscs with the proposed crystal structures.

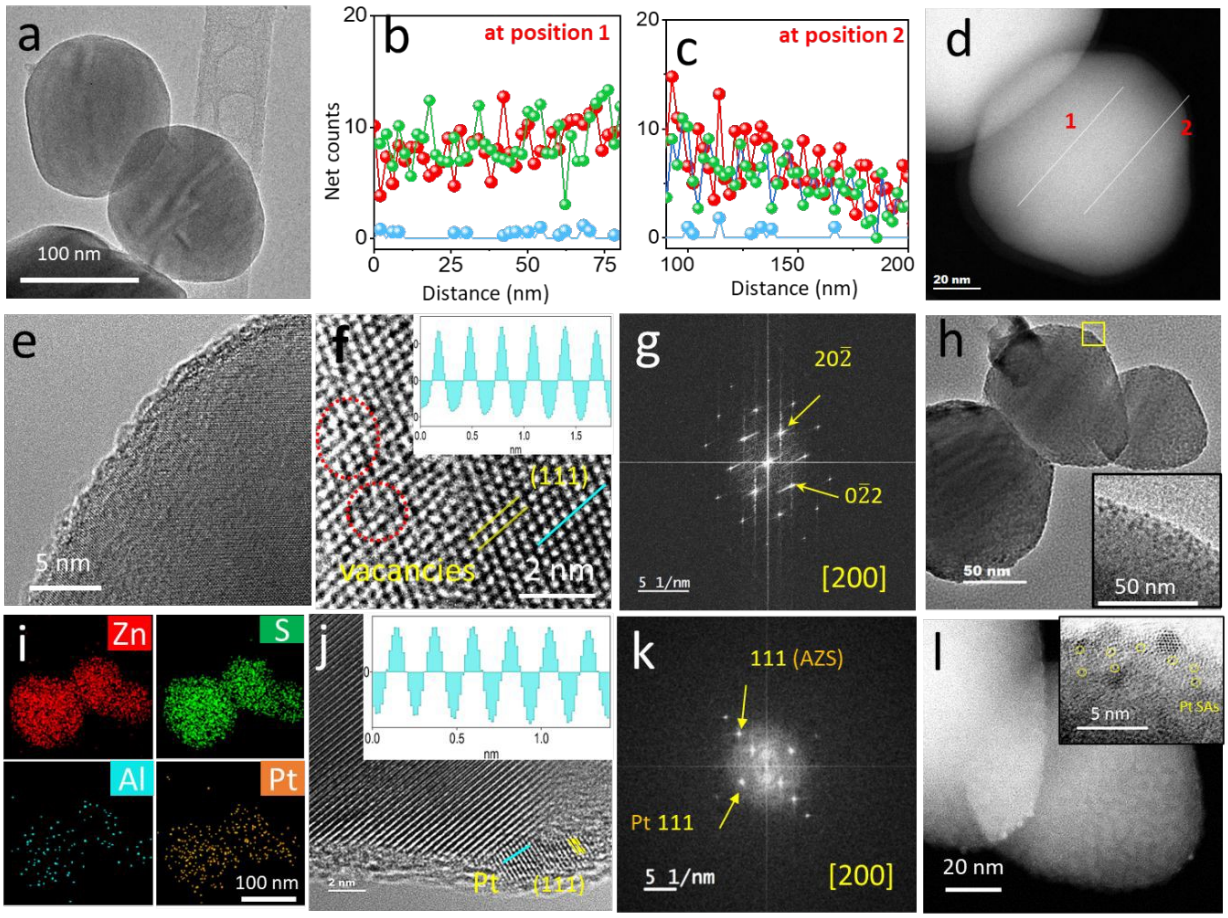

Fig. 2 a) TEM image of AZS; b-c) EDS line scan profiles of AZS measured at the middle (position 1) and corner position (position 2) of AZS, respectively. The plots for Zn, S and Al were shown in red, green and blue colors, respectively. d) The dark field-TEM image of AZS; e) HRTEM image of AZS; f) STEM image of AZS showing atomic arrangement. Inset shows line profile for interplanar spacing of (111) planes of AZS. g) Simulated SAED pattern of STEM image of AZS in f); h) TEM image of Pt-AZS. Inset image shows Pt SA decoration on AZS. i) Elemental mapping of Zn, S, Al and Pt in Pt-AZS; j) STEM image of Pt-AZS showing the Pt SA sites on AZS. Inset shows line profile for interplanar spacing of (111) planes of Pt. k) Simulated SAED pattern of STEM image of Pt-AZS in j); l) The dark field-TEM image of Pt-AZS. The HRTEM in inset shows Pt SA sites (encircled black dots) on AZS.

Journal of Materials Chemistry A Accepted Manuscript

View Article Online
DOI: 10.1039/D5TA02703F

Published on 28 August 2025. Downloaded by National Yang Ming Chiao Tung University on 9/8/2025 8:16:04 AM.

Journal of Materials Chemistry A Accepted Manuscript

arrangement in STEM (Fig. 2f) of AZS show zinc blend ZnS structures (JCPDS Card No. 65-0309)[42] grown in a single crystalline orientation along the (111) lattice plane with an interplanar spacing (d) of 0.31 nm (line profile for interplanar distances from HRTEM are shown in the inset of Fig. 2f).[43] This single crystalline growth is also confirmed from the simulated selected area electron diffraction (SAED) pattern of the STEM image of AZS (Fig. 2g). As seen from the TEM of Pt-AZS (Fig. 2h), AZS retains its morphology even after the Pt photodeposition process. The STEM image in Fig. 2h reveals growth of tiny single crystalline Pt nanocrystals (~ 2 nm) on the (200) lattice plane of AZS with uniform surface decoration, as seen in the inset of the TEM in Fig. 2h.

In Fig. 2i, the EDS mappings of Pt-AZS (the corresponding TEM image is shown in Fig. 2h) showed uniform elemental distribution of Zn, S, Al, and Pt, which support the formation of disc-like shape of AZS. No degradation or oxidation seen for Pt-AZS after photodeposition which is confirmed from O level in its EDS Spectrum (Fig. S3f). The growth of Pt on the S-rich (200) plane of AZS at the atomic scale is shown by the STEM image of Pt-AZS (Fig. 2j). The inset of Fig. 2j represents the line profile for d-spacing of 0.25 nm corresponding to the (111) lattice plane of Pt, which is also reflected in its SAED pattern (Fig. 2k).[44] Fig. 2l shows the HAADF-STEM image of Pt-AZS. Because the contrast is proportional to the square of the atomic number, the uniformly distributed tiny bright spots that emerged in the dark-field TEM of Pt-AZS indicate deposition of Pt SA sites.[45]

The generalized gradient approximation (GGA) in the formalism of Perdew-Burke-Ernzerhof (PBE) was adopted to describe the electronic exchange-correlation energy. The projector augmented wave (PAW) pseudo-potentials were chosen to describe ionic cores.[46,47] We have utilized the standard PBE functional method which improved the van der Waals interactions correctly by Becke-Jonson damping potential with the DFT-D3 method.[48] The convergence criterion for the self-consistent iteration was 10-5 eV. The calculations were carried

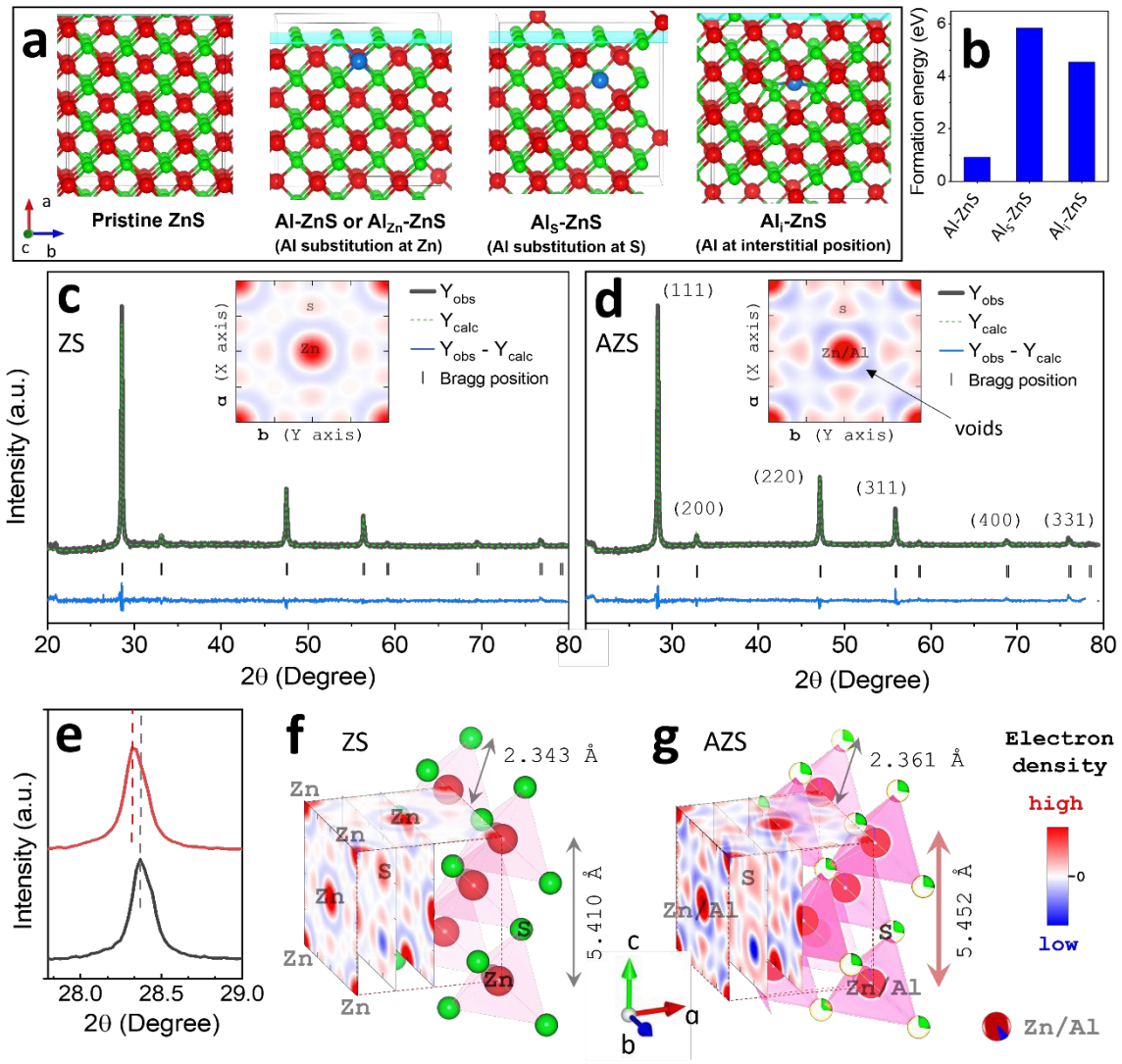

Fig. 3 a) Supercell of pristine ZnS and Al-doped ZnS with Al at substitutional position of Zn, substitutional position of S and interstitial position, respectively, b) histogram plot for comparison of their formation energies using DFT calculations, (c) Rietveld refinement of XRD data of ZS; d) Rietveld refined data of AZS with Al substitution at Zn 4a sites. The insets of a) and b) show EDMs at x = 0 along [100] axis for ZS and AZS, respectively. e) Enlarged XRD (111) peaks with lower angle shift for AZS than for ZS; f, g) The distributions of electron densities in unit cells of ZS and AZS, respectively.

This journal is © The Royal Society of Chemistry 20xx

Please do not adjust margins

View Article Online
DOI: 10.1039/D5TA03731

Published on 28 August 2025. Downloaded by National Yang Ming Chiao Tung University on 9/8/2025 8:16:04 AM.

Journal of Materials Chemistry A Accepted Manuscript

out with a plane-wave basis set cutoff energy set to 520 eV with a Gaussian smearing method of 0.05 eV width in order to assure well-converged total energy and force values.

The structural optimization of the cubic $\bar{F}43m$ space group (216) of the ZnS crystal structure was performed with the k-point mesh with the Monkhorst–Pack scheme set to 4×4×4. The predicted lattice parameters of unit cell are 5.383 Å, in good agreement with the experimental data (a=b=c=5.409 Å). To model the Al-doped material, we considered a ZnS supercell (2x2) model containing 32 ZnS units and the cell parameters a=b=c=10.760 Å. We considered two possible ways of introducing Al-doping into the lattices of ZnS. The first was a Zn or S atom substituted with an Al atom (denoted by Al_{Zn} and Al_S); the second was an Al doping atom situated in an interstitial position (denoted as Al_{int}). To characterize the stability of the dopant in substitutional and interstitial configurations in ZnS, we calculated the formation energies (E_{form}) using the following relation $E_{form} = E(Al\text{-}ZnS) - E(ZnS) - \mu(Al) + \mu(Zn)$, where E(ZnS) and E(Al-ZnS) are the total energies of the pristine ZnS supercell and doped ZnS. The quantities μ(Al), μ(Zn), and μ(S) represent the chemical potentials of aluminum and the substituted Zn or S atom in the host lattice, respectively. The chemical potential for doping μ(Al), μ(Zn), and μ(S) is calculated from the Al, α-Solid S8, and Zn bulk metal, respectively. The formation energies of dopant atom in different configurations were calculated by using the DFT-D3 method and presented in Table 1. The supercell model and partial geometries from the structurally optimized Al-doped ZnS are shown in **Fig.3a**. We observed that the resulting Zn substituted with an Al atom to form Al-ZnS expands the lattice.

We theoretically investigate the formation energy of Al substituted with Zn in ZnS, which is 0.93 eV, relatively more stable than other doping sites. The substituted optimized supercell lattice constant of the axis slightly increased to 10.793 Å from 10.760 Å in that of the ZnS (see Fig. 3a). In our calculations, we observed that the formation energy of Al substituted at the S site in the ZnS model (5.85 eV) indicates a higher formation energy than Al substituted at the Zn site (0.93 eV). For comparison, we also calculate the Zn defect formation energy in the ZnS, which is 3.58 eV, much lower than the S defect (4.15 eV). In the Al atom interstitial model (Al_{int}), we have investigated the effect of Al doping located interstitially at various places in between the S and Zn of ZnS supercell, and their formation energy is 4.56 eV. These results indicate that the Al substitution at Zn in ZnS is relatively more stable than other doping sites and therefore a more favorable doping site. Moreover, the electronic structure of Al_{Zn}-ZnS (i.e., AZS) is modified due to the lattice expansion with the Zn-S bond length increased from 2.33 Å to 2.34 Å. The similar increase in Zn-S bond distance was observed from the Rietveld refinement of experimental XRD data in subsequent discussion.

The 2.2 % of Al doping was found to be sufficient to produce lattice distortion of the ZnS unit cell (XRD pattern in Fig. 3c and d). These XRD patterns show sharp diffraction peaks indexed to the F-43*m* group of the zinc blend ZnS structure, which enables sufficient space for doping by bigger-sized cations. In AZS (Fig. 3d), the intense peak at 28.4° of the (111) lattice plane and the small peak at 32.9° of the (200) lattice plane reflects a preferential crystal growth along the (111) plane bounded by the (200) facet plane and contribute to the nanodisc morphologies derived from the HRTEM analysis. Since the atomic radius of dopant Al (143 pm) is a little bigger than that of Zn (137 pm), it has induced lattice expansion in the cubic ZnS unit cell. Therefore, an unambiguous peak shift toward lower angles was observed (Fig. 3e). The resultant increase in lattice constants (Figs. 3f and 3g) is extracted from the XRD Rietveld refinement of both ZS and AZS (Fig. 3c and 3d). The pristine ZnS showed the F-43*m* space group, where Zn occupies the 4α:0 0 0 and S occupies the 4b:¼ ¼ ¼ Wyckoff positions, respectively.[49] The zinc blend wurtzite crystal structure allows sufficient space for cation doping, in which three possible sites are available for Al-doping, namely the Zn-site, the S-site and the interstitial position.[40] However, Al doping in the interstitial position is a less favorable and unstable phase. During the formation of the zinc blend structure, the 4α sites (corresponding to Zn) are available for Al^{3+} cation occupation, and therefore refinement was done by considering Al SA doping at some of the 4α:0 0 0 positions. The fitting converges well after the inclusion of the crystalline anisotropy coefficient for the dominant (111) plane. The 2.2 % doping of relatively bigger Al cations causes a slight shift of (111) peaks towards smaller angle, indicating expansion in the unit cell with an increment of 0.042 Å in each lattice constant, as seen from Figs. 3d and 3e. An increase in Zn-S bond length from 2.343 Å to 2.361 Å on Al SA doping is observed, which makes the Zn-S bond in AZS weaker than that in ZS. The SA doping is also detected from EPR spectra of ZS and AZS, which showed weakening of AZS EPR intensity due to the Zn vacancy filling by Al atoms. The Al SA doping lowers the interaction between vacancies (Fig. S4a).[26]

The Fourier electron density mapping (EDM) in ZS and AZS was generated by taking projections along the [100] axis taken at different cross-sections of the unit cell with contour color representing the strength of electron densities. From the inset of Fig. 3c, the higher electron density is observed around cations (Zn/Al) than that around S (warm region in red color), while the lowest electron density is seen in neighboring crystal voids (cool region in blue color).[50,51] In AZS, the increase in Zn-S bond length enhanced the electron charge distribution around atoms and also increased the void volume (inset of Fig. 3d). Eventually, this leads to influence on the band edge positions and optical properties of AZS, which will be elaborated on in the next section. In hydrothermal synthesis, Al^{3+} was found to be a good option for doping due to its less affinity towards phase formation with S at modest reaction temperatures. Furthermore, Al^{3+} can introduce additional defect levels near CB that may delay carrier recombination. Note that no lattice distortion was found after the addition of NaCt (a reducing agent) during ZnS synthesis, which is confirmed by comparing the XRD patterns of ZS0 (Figs. S4b-c) and ZS (Fig. 3c) and revealing the same lattice parameters with identical EDM.

The X-ray photoelectron spectroscopy (XPS) was utilized to determine the chemical states and surface element composition of ZS and AZS (Figs. S5, S6 and S7). Usually, the

Please do not adjust margins

View Article Online
DOI: 10.1039/D5TA03971

Published on 28 August 2025. Downloaded by National Yang Ming Chiao Tung University on 9/8/2025 8:16:04 AM.

Journal of Materials Chemistry A Accepted Manuscript

incorporation of dopant can increase the charge carrier density in photocatalysts, which ultimately affects their XPS peak positions.[26] After ~12% Cu doping in ZnS, Liu et al. observed 0.29 eV and 0.19 eV shifts towards higher binding energy (BE) in Zn 2p and S2p XPS peaks, respectively, indicating the introduction of additional charge carriers. While, under light irradiation, decreases in BEs of these peaks were seen due to the transfer of photoexcited electrons to surface metal atoms/cocatalysts via the Mott-Schottky interface.[52] The previous investigations have shown that SA sites may extract photogenerated electrons and lower the electron density (charge carrier) in the photocatalyst, while the intrinsic doped metal atoms serve as electron-transfer bridges with increased charge density.[26,53,54] The present Pt-AZS photocatalyst includes both intrinsic metal atom doping as well as Pt SA decoration on the AZS surface. Specifically, after comparing core levels of ZS and AZS, the BE intervals between $2p_{3/2}$ and $2p_{1/2}$ peaks for both Zn and S remained unchanged, which manifests intactness of the parent zinc blend structure. The quantitative XPS analysis of ZS and AZS survey spectra revealed that the Al atom preferentially replaces its adjacent S atoms to create S vacancies (Fig. S5). As shown in the XPS scan spectrum of Pt-AZS (Fig. S7c), the peaks observed at 71.4 eV and 76.8 eV are associated to the $4f_{7/2}$ and $4f_{5/2}$ orbitals of Pt, respectively, while a minor peak at 73.9 eV corresponding to the Al 2p core level confirms the small amount of Al doping in Pt-AZS. The chemical states are determined from observed BEs of the core level of elements. The BE peak at 1021.3 eV corresponds to the Zn $2p_{3/2}$ core level with a +2 oxidation state, while the major peak at 161.3 eV confirms S $2p_{3/2}$ with a -2 oxidation state. A small peak observed near 73.9 eV reveals the Al 2p core level with a +3 oxidation state. Similarly, the characteristic peak at 71.4 eV, corresponding to Pt $4f_{7/2}$, confirms deposition of metallic Pt (Pt^0) on AZS, while the BE peak at 76.8 eV, corresponding to Pt $4f_{5/2}$, has a +2 valency.

3.2. Photoactivation of Pt-AZS in water vapor and in-situ XPS study

The in-situ XPS measurements were conducted under light irradiation to investigate the relative kinetics of photogenerated electrons in the Pt-AZS system (**Fig. 4**). The XPS measurements performed in dark (W) and under light irradiation (WL) with corresponding plots for Zn, S, O, and C peaks are shown in Figs. 4a-4d, respectively. In-situ measurements performed every 2hs are plotted as WL-4h, WL-6h and WL-8h, as shown in Figs. 4e and 4f. In Pt-AZS, as only 1.6 wt% Pt was utilized for decoration, the low-concentrated Pt SA sites will not influence the metal-sulfide XPS peaks appeared near 161.3 eV. When comparing XPS spectra of bare Pt-AZS with those under light irradiation, both Zn $2p_{3/2}$ and Zn $2p_{1/2}$ peaks were equally shifted by 0.4 eV towards lower binding energies compared to those in dark conditions (Fig. 4a). The similar lower energy peak shift of 0.4 eV was detected in S 2p core levels. These downshifts in binding energies predict that the photogenerated electrons are more likely to be trapped by the defect levels (S vacancies and shallow defect levels as electron gathering centers) and then transferred to the Pt SA sites grown on the S-rich (200) facet of Pt-AZS.[55] The two minor peaks observed at 165.7 eV and 167 eV in Pt-AZS (Fig. 4b) are attributed to a $–C–(SO_2)–C$ sulfone bridge.[56] Notably, throughout the in-situ photocatalytic study, the water vapor was generated by controlled water sprinkling in the XPS chamber at a fixed vacuum level (~2×10^{-2} Torr). In the dark, the O1s core level has two peaks at 530.5 eV and 532.2 eV, corresponding to the C=O and C-O species of TEOA, respectively.[57] The XPS peak seen at 533.8 eV is associated with C-OH. With continual purging of water vapors, an additional peak contributes at 535.0 eV, which steadily increases in intensity over time.[58,59] The effect of light irradiation on adsorbed TEOA was investigated by monitoring in-situ XPS spectra of O 1s (Fig. 4c), C 1s (Fig. 4d), and N 1s core levels (Fig. S7d). The positions of intense peaks of O 1s and N 1s were unshifted after light exposure that revealed chemical stability of the TEOA molecules. In contrast, the lower BE shift of 0.5 eV in C 1s occurred by capturing photoinduced holes from Pt-AZS to produce $TEOA^+$. This in-situ XPS analysis explains the improved photogenerated electron transfer mechanism from the CB of AZS to Pt SA sites. In addition, the shallow trap levels created by Al-doping can also be contribute to photogenerated electron harvesting and subsequent transfer to Pt sites, which will be discussed in the following section. These shifts in BEs remained unchanged on continuous light exposure (Fig. 4e & 4f), indicating chemical stability of Pt-AZS in full light spectra.

3.3. Photocatalytic H_2 evolution performance

The photocatalytic H_2 evolution performances of Pt-decorated pristine ZnS (ZS0 and ZS) and Al-ZnS (AZS) in an aqueous solution of 10 vol% TEOA (sacrificial agent) were investigated under AM 1.5G solar spectral irradiation (**Fig. 5**). Figs. 5a and 5b exhibit enhancement in H_2 production after Al-doping. The Pt-loaded pristine photocatalysts ZS0 and ZS showed low H_2 production yields of 2.6 and 11.3 mmol g^{-1} h^{-1}, respectively, whereas the S-vacant Pt-AZS has an improved H_2 evolution rate up to 17.1 mmol·g^{-1}·h^{-1}. Pt-AZS exhibits increased photocatalytic activity due to the rapid photocarrier separation caused by the S vacancies acting as electron traps. Additionally, Pt SA sites boosted H_2 evolution activity by increasing electron extraction from AZS to Pt SA through Mott-Schottky heterojunction under light irradiation. Herein, 1.6 wt% Pt deposition was observed on the AZS surface (confirmed from EDS analysis). After simulated solar irradiation, the prepared Pt-AZS was recycled several times and studied for its H_2 evolution performance (Fig. S9). For the comparison purpose, under similar conditions, the H_2 evolution performance of TiO_2 nanoparticles (~20 nm, P25) was investigated, which showed only a 13.5 mmol$g^{-1}h^{-1}$ yield. The photocatalytic quantum efficiencies of Pt-AZS were investigated by measuring photocatalytic H_2 evolution for monochromatic band-pass (BP) filters of different wavelengths (λ = 420, 400, 380, 365 (WB50), and 345 (WB40) nm). The total H_2 evolution and the total number of photons transmitted by these band-pass filters are provided in Table S2. Accordingly, the AQY of Pt-AZS for these wavelengths was calculated (the details of the

 This journal is © The Royal Society of Chemistry 20xx

Please do not adjust margins

View Article Online
DOI: 10.1039/D5TA03793J

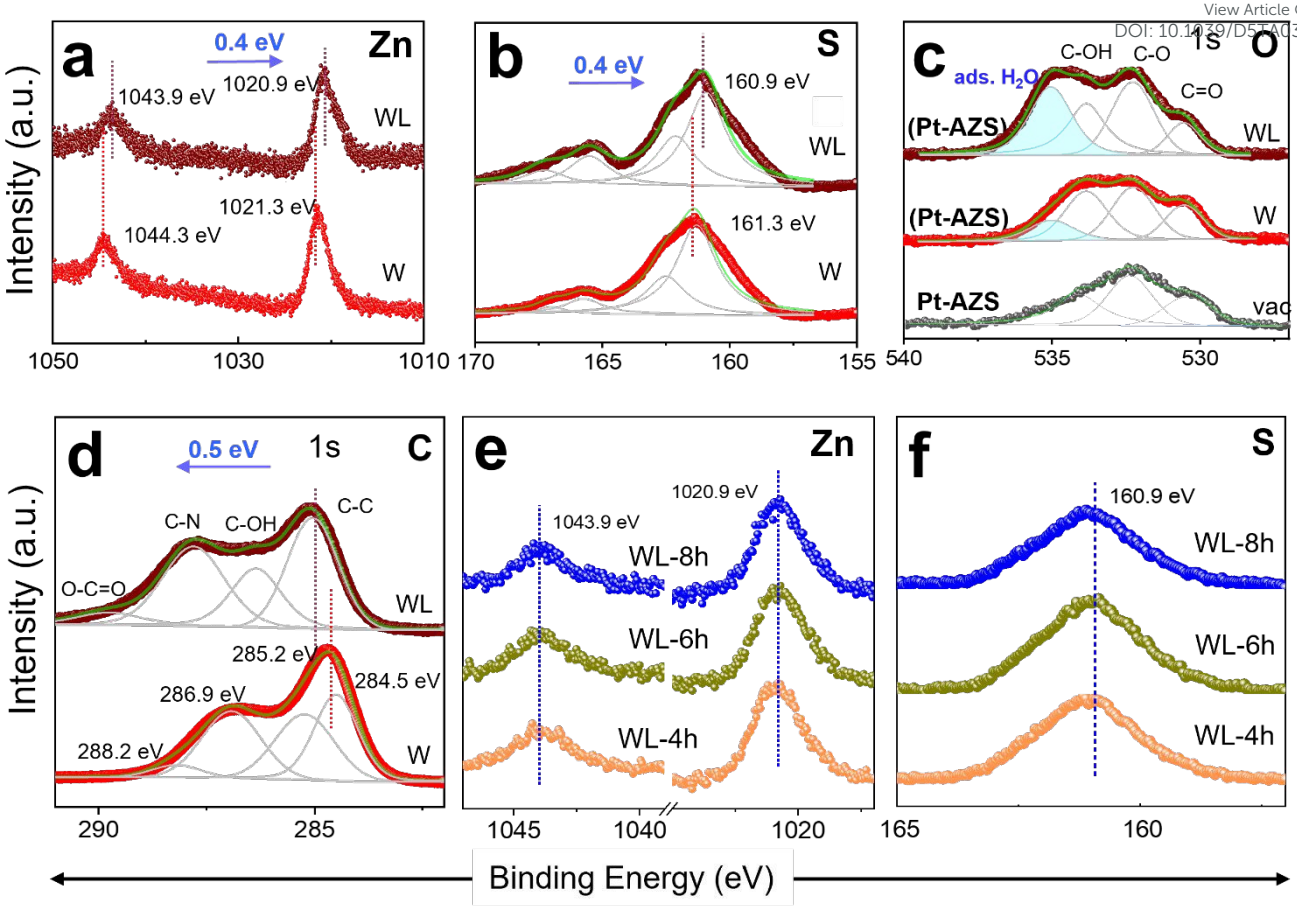

Fig. 4 The in situ XPS spectra for a) Zn 2p, b) S 2p, c) O 1s and d) C 1s in the presence of water vapors (W) and under light irradiation (WL) on TEOA adsorbed Pt-AZS film. e, f) The XPS peak positions of Zn and S under light after 4, 6 and 8 h of irradiations.

calculations are provided in Supporting Information), and the H_2 evolution rate histograms were plotted in Fig. 5c.

The transmitted light intensity profiles of the BP filters are also plotted on the inverted X-axis. The observed AQYs are 0.02% (420 nm), 0.05% (400 nm), 0.04% (380 nm), 0.35% (365 nm), and 34% (345 nm), where these histograms coincide with its UV-Vis absorbances. These values demonstrate the excellent UV activity of Pt-AZS, and therefore, an H_2 evolution study was conducted in a two-channel photoreactor with provision of UV-A and UV-B lamps (Fig. S10). As depicted in Fig. 5d, Pt-AZS showed the highest H_2 evolution rate of 38 mmol g^{-1} h^{-1}; in contrast, under the same experimental conditions, Pt-ZS has reached only 21.4 mmol g^{-1} h^{-1} which manifests the superior HER activity of Pt-AZS in the UV region. The stability of Pt-AZS was confirmed by conducting H_2 evolution experiment for 48h under illumination of simulated solar spectra. After 48hr the sample color remains same but TEOA color changed to yellow due to formation of $TEOA^+$ (Fig. S11). This post-photocatalytic sample was denoted by Pt-AZS-48h which is further characterized for XRD, XPS, TEM and EDS (with mapping) measurements. The XRD of Pt-AZS-48h showed no change in peak positions which indicates no degradation of sample on Pt-deposition (Fig. S12). The stability of sample was visualized from EDS spectrum where no O-peak appeared after prolong use in solvent under light illumination (Fig. S13). The uniform elemental distribution was seen from EDS mapping in Fig S13c. The O-level in the pre- and post-photocatalytic reaction was determined by measuring XPS spectra of AZS, Pt-AZS and Pt-AZS-48h on C-tape (Fig. S14). The ratio of C/O describes the O level and hence stability of prepared samples. Interestingly, for all these conditions, C/O remains nearly same except for high Al doped AZS* where, C/O is 0.159 indicating possible secondary oxide phase (table S3). Furthermore, the EDS spectra of above samples with elemental mapping confirms least O level while uniform distribution of other elements (Fig S15).

3.4. Band structure, charge-transfer dynamics and photocatalytic mechanism for H_2 evolution

To understand the source of enhanced photocatalytic activity of AZS for H_2 evolution, the fundamental processes such as absorption/PL spectra, charge separation, and photogenerated electron transfer were further studied. Ultraviolet photoelectron spectroscopy (UPS) technique has been utilized to predict the band structures for ZS and AZS. By using the formula $\Phi = h\nu - (E_{cutoff} - \Phi_{Au})$, work functions ($\Phi$) for ZS and AZS are determined to be -2.89 eV and -3.37 eV, respectively, where $h\nu$ is the photon energy 21.22 eV, E_{cutoff} is cutoff energy, and Φ_{Au} is the work function of Au to be determined by UPS shown in Fig. S16b.[30,60] Using values of Φ and binding energies (E_b) from Fig. S16c, the valence band maxima (VBM) are

Published on 28 August 2025. Downloaded by National Yang Ming Chiao Tung University on 9/8/2025 8:16:04 AM.

Journal of Materials Chemistry A Accepted Manuscript

Please do not adjust margins

View Article Online
DOI: 10.1039/D5TA03793J

Published on 28 August 2025. Downloaded by National Yang Ming Chiao Tung University on 9/8/2025 8:16:04 AM.

Journal of Materials Chemistry A Accepted Manuscript

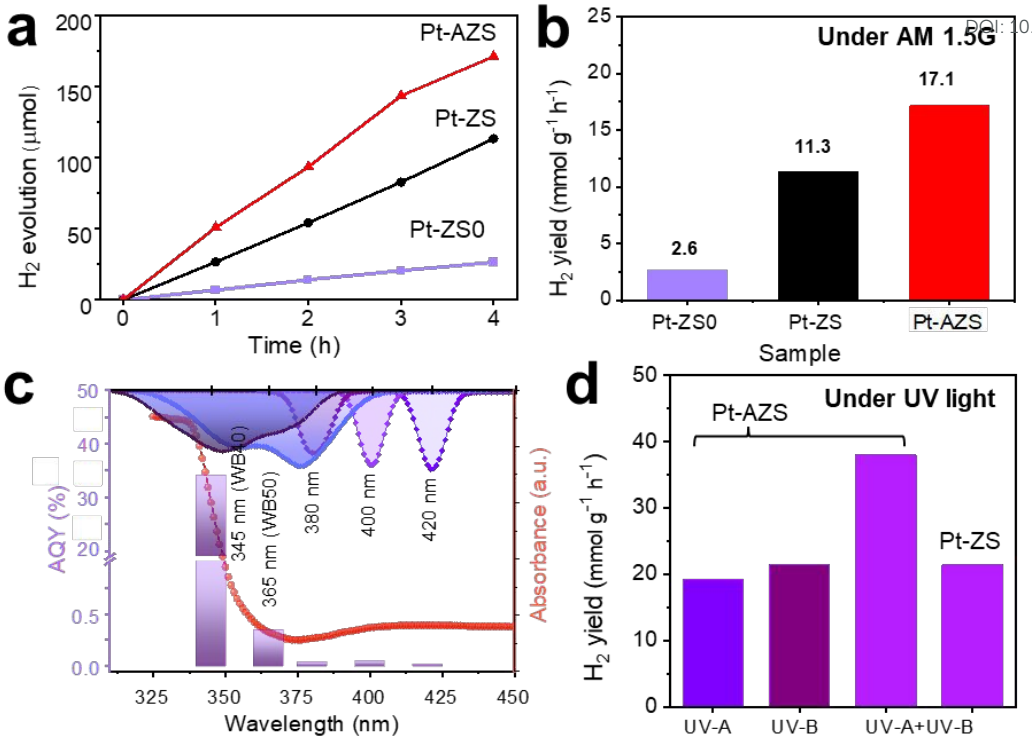

Fig. 5 a) H_2 evolution performance with time; b) Rate of H_2 production by Pt-ZS0, Pt-ZS and Pt-AZS under AM1.5G light irradiation; c) Apparent quantum yield (AQY) under different wavelengths using narrow band (NB), wide band (WB) spectral filters; d) The H_2 evolution rates of P-ZS ad Pt-AZS under UV-A, B irradiation.

estimated to be -6.36 eV for ZS and -5.77 eV for AZS.[61] Accordingly, their conduction bands are determined by adding E_g to the VBM values. The 2.2 % Al-doping upshifted VB (and CB) towards the vacuum level by 0.59 eV more than that of pristine ZS, while the Fermi level went down by 0.48 eV (Fig. S16d). UPS of pristine ZnS (ZS*), the cutoff energy positions were shown in Fig. S17.

The defect states can also contribute in the quenching of carrier recombination. Photoluminescence (PL) spectroscopy can be applied to investigate these defect states from the analysis of radiative recombination of photogenerated electrons and holes.[62] As illustrated in the PL spectra of AZS (Figs. S18a and 6a), the higher excitation wavelengths (λ_{ex} > 340 nm with energy lower than E_g) enhance the blue emission (425-470 nm), while suppressing broad orange emission near 600 nm. Particularly, for the low excitation energies (below E_g), the increase in intensities of shorter wavelength PL peaks observed over the range of 420-520 nm indicates a considerably higher recombination rate of photogenerated electrons, which gives evidence of poor charge separation. The PL peak intensities of AZS are weaker than the PL peak intensities of AZS are weaker than those of pristine ZS, attributed to the suppression of charge recombination after Al-doping. The incorporation of Al in ZnS can efficiently segregate the photoexcited charge carriers and improve the photocatalytic efficiency of the photocatalyst by quenching the recombination of the photogenerated electrons by means of intermediate defect levels. After comparing deconvoluted PL spectra of ZS and AZS obtained at 340 nm excitation, an additional peak emerged at 535 nm, while a dominant peak at 606 nm was suppressed after Al doping (**Fig. 6**). As shown in Fig. 6b, the PL spectra indicate significant changes due to Al doping. emissions are explained by the simplified picture of different defect centers, namely, S vacancy (V_S), Al SA substitutional defects (I_{Al}), and zinc defects (V_{Zn}). The three blue emissions observed at 425, 441, and 465 nm are attributed to radiative de-excitation of photogenerated electrons from the defect state of S vacancies, while a green emission at 501 nm can be originated by the direct transition from the CB edge to the V_{Zn} level.[27] Similarly, the dominant broad orange emission peak at 606 nm is assigned to the transition of electrons from interstitial Zn (I_{Zn}) defect states to V_{Zn} (deep level transitions). Usually, cation substitutional defects (I_{Al}) are located near CB, and the new peak that appeared at 535 nm can arise due to the self-activated luminescence by I_{Al}-V_{Zn} transitions (shallow trap-acceptor level transitions), which is a characteristic peak of substitutional doping.[37,63] Furthermore, the peak suppression at 606 nm emphasizes a substantial reduction in I_{Zn} states and subsequently enhances electron trapping at V_S states.

To elucidate the charge carrier dynamics, the TRPL decay profiles of ZS and AZS were obtained by laser pumping at λ_{ex} = 375 nm. The TRPL spectra of thin films shown in Fig. 6c are well fitted to the tri-exponential decay function $I(t) = A_1 e^{-t/\tau_1} + A_2 e^{-t/\tau_2} + A_3 e^{-t/\tau_3}$, where I represents the PL intensity, A_i the percent contribution, and τ_i (i = 1-3) lifetime components. The estimated parameters derived from fitted curves are demonstrated in Table S4. The average lifetime (amplitude weighted) of AZS is 2.50 ns, which is longer than that of ZS (2.26

This journal is © The Royal Society of Chemistry 20xx

Please do not adjust margins

View Article Online
DOI: 10.1039/D5TA03793J

Published on 28 August 2025. Downloaded by National Yang Ming Chiao Tung University on 9/8/2025 8:16:04 AM.

Journal of Materials Chemistry A Accepted Manuscript

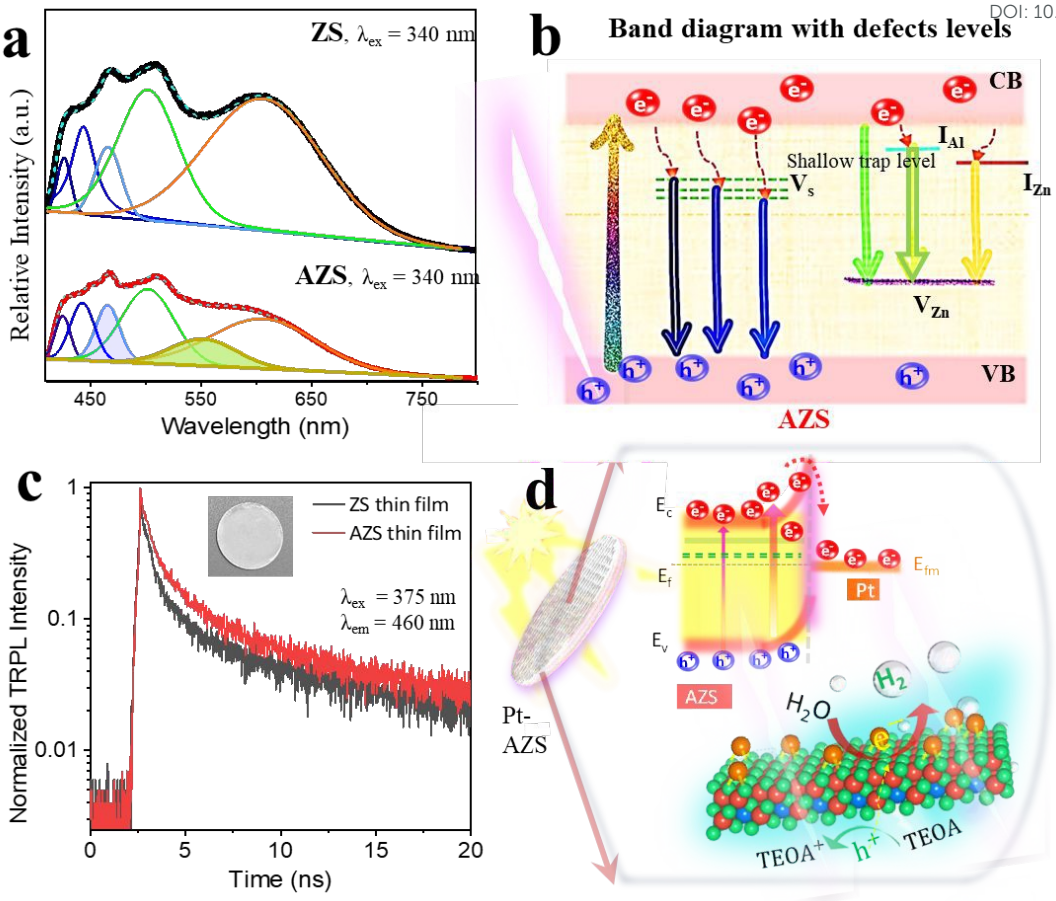

Fig. 6 a) Comparison of PL emission spectra of ZS and AZS at λex = 340 nm; b) Schematic of energy level diagram with shallow trap level, S vacancy and zinc defect states; c) TRPL decay curves of the thin film samples; d) Photocatalytic charge transfer mechanism in AZS/Pt Mott-Schottky junction under light irradiation in 10 vol% TEOA aqueous solution.

ns). Moreover, the contribution of long-lived excited electrons (with longer lifetime component τ_3) in AZS is higher (45%) than its counterpart in ZS (20%), indicating preferential migration of photogenerated carriers to the electron traps for efficient charge transport rather than its recombination, which is attributed to increased defect levels after Al-doping. Based on the fractional amplitudes of lifetime components, a shorter PL lifetime of non-radiative transition represents fast transfer of photogenerated electrons to the defect states prior to its radiative decay process. Further, the electron transfer dynamics can be analyzed without interrupting long-lived radiative recombination by conducting TRPL measurements of catalysts in aqueous suspension (Fig. S18b). The observed TRPL data follows the biexponential trend I(t) = $A_1e^{-t/\tau_1}+A_2e^{-t/\tau_2}$ with average PL lifetimes of 1.63 ns and 1.95 ns for ZS and AZS, respectively. Table S5 gives the estimates of amplitudes and lifetime components for aqueous dispersion of ZS and AZS. For aqueous suspension of photocatalysts, the photoexcited electrons with longer lifetime (τ_3) are efficiently transported to Pt SA sites via the Schottky interface for water reduction. Therefore, only electrons with shorter lifetime (τ_1 and τ_2) exhibited recombination. The short lifetimes components τ_1 could arise from non-radiative transition from CB to the different trap levels near CB, while component τ_2 corresponds to recombination of photoprompted electrons from V_S to VB.

Based on the above discussion, the mechanism of photoexcitation and electron transport from the CB of AZS to Pt SAs through the Mott-Schottky junction is shown in Fig. 6d; two possible H_2 production mechanisms are shown in Fig. S19. The irradiation of light on aqueous dispersion of AZS excited electrons to CB, while holes are mitigated by TEOA, forming $TEOA^+$ ions. In AZS, the shallow defect levels and Vs states efficiently trap the photopromted electrons and delay their recombination while downshifting in E_f has lowered band bending after the Mott-Schottky junction, which enhanced the probability of electron transport to the Pt SA sites. On the other hand, the elevated conduction band (CB) of AZS provides a greater reduction capability for the photogenerated electrons and enhances the formation of molecular hydrogen compared to undoped ZS. These favorable modifications in the AZS band structure leads to an enhanced H_2 evolution under both AM1.5G and UV light irradiation with degradation of its single crystallinity. The additional shallow donor states introduced by Al-doping enhanced the electron traps and increased the average lifetime of high-energy electrons, while Pt SA sites of

Please do not adjust margins

View Article Online
DOI: 10.1039/D5TA03231

Published on 28 August 2025. Downloaded by National Yang Ming Chiao Tung University on 9/8/2025 8:16:04 AM.

the S-rich (200) facet served as electron wells on photoexcitation.

4. Conclusions

The limited photocatalytic activity of wide bandgap ZnS could be enhanced by controlled Al SA doping for regulating the trap states in band structure and modulation of electron transport. Owing to the asymmetric single crystalline growth exposing the (200) facet and the change in electron density by lattice expansion, the favorable migration of photoexcited electrons to the S-rich (200) plane provides an extra driving force for immobilization of Pt SA sites onto the basal plane of AZS. Moreover, Al-induced donor levels (shallow defects) can increase the lifetime of photoprompted electrons and improve charge transport. With an enhanced photon absorption by a single crystalline AZS planar surface, a bulk excitation and transport of electrons to Pt exhibit an improved H_2 evolution rate of 17.1 $mmolg^{-1}h^{-1}$ under AM1.5G irradiation, which is 33% higher than the pristine ZS. The Pt-AZS has achieved an AQY of 34% at an exposure of a monochromatic light at 345 nm by using a WB40 UV filter. The further improvement in H_2 yield is achieved by irradiating the system in a two-channel photochemical chamber (under UV-A and UV-B exposure), showing a best HER rate of 38 mmol g^{-1} h^{-1} for Pt-AZS, which is two times more than that of Pt-ZS. The donor level incorporation by Al-doping without sacrifice of single crystal structure and anisotropy of ZnS is demonstrated. The lack of grain boundaries in AZS single crystalline growth with a favorable S-rich bed has offered the rapid photoexcitation of electrons on the (200) facet from the bulk. This work renders insights for an improved photocatalytic H_2 evolution by Al-doping in single crystalline photocatalysts, which may modulate electronic band structure and defect states to gain a remarkable solar-to-hydrogen production efficiency better than any reported values.

Author contributions

The manuscript was written through contributions of all authors. All authors have given approval to the final version of the manuscript.

Conflicts of interest

The authors declare no conflict of interest.

Data availability

The data that support the findings of this study are available from the corresponding author upon reasonable request.

Acknowledgements

The authors are grateful to Dr. Y.-C. Lee and Ms. P.-Y. Huang (TLS 14A1, NSRRC) for their valuable assistance with IR data analysis.

We gratefully acknowledge the support by the National Science and Technology Council (NSTC), Taiwan (grant No. NSTC 113-2639-M-A49-001-ASP and NSTC 114-2639-M-A49-001-ASP), the Center for Emergent Functional Matter Science of National Yang-Ming Chiao-Tung University (NYCU) from the Featured Areas Research Center Program within the framework of the Higher Education Sprout Project by the Ministry of Education (MOE) in Taiwan.

Footnote

† Electronic supplementary information (ESI) available. See DOI: https://doi.org/10.1039/x0xx00000x

References

1 1 W. H. Lee, C. W. Lee, G. D. Cha, B.-H. Lee, J. H. Jeong, H. Park, J. Heo, M. S. Bootharaju, S.-H. Sunwoo, J. H. Kim, K. H. Ahn, D.-H. Kim and T. Hyeon, *Nat Nanotechnol*, 2023, **18**, 754–762.
2 2 Y. Chen, L. Soler, C. Cazorla, J. Oliveras, N. G. Bastús, V. F. Puntes and J. Llorca, *Nat Commun*, 2023, **14**, 6165.
3 3 J. Ding, W. Yan, S. Sun, J. Bao and C. Gao, *ACS Appl Mater Interfaces*, 2014, **6**, 12877–12884.
4 4 B. Dai, J. Fang, Y. Yu, M. Sun, H. Huang, C. Lu, J. Kou, Y. Zhao and Z. Xu, *Advanced Materials*, 2020, **32**, 1906361.
5 5 T. Hisatomi and K. Domen, *Nat Catal*, 2019, **2**, 387–399.
6 6 Z. Lian, Z. Li, F. Wu, Y. Zhong, Y. Liu, W. Wang, J. Zi and W. Yang, *Commun Chem*, 2022, **5**, 93.
7 7 Z. Wang, Y. Luo, T. Hisatomi, J. J. M. Vequizo, S. Suzuki, S. Chen, M. Nakabayashi, L. Lin, Z. Pan, N. Kariya, A. Yamakata, N. Shibata, T. Takata, K. Teshima and K. Domen, *Nat Commun*, 2021, **12**, 1005.
8 8 Z. Fang, S. Weng, X. Ye, W. Feng, Z. Zheng, M. Lu, S. Lin, X. Fu and P. Liu, *ACS Appl Mater Interfaces*, 2015, **7**, 13915–13924.
9 9 C.-W. Tsao, S. Narra, J.-C. Kao, Y.-C. Lin, C.-Y. Chen, Y.-C. Chin, Z.-J. Huang, W.-H. Huang, C.-C. Huang, C.-W. Luo, J.-P. Chou, S. Ogata, M. Sone, M. H. Huang, T.-F. M. Chang, Y.-C. Lo, Y.-G. Lin, E. W.-G. Diau and Y.-J. Hsu, *Nat Commun*, 2024, **15**, 413.
10 10 J. He, B. Li, J. Yu, L. Qiao, S. Li, X. Zu and X. Xiang, *Opt Mater (Amst)*, 2020, **108**, 110231.
11 11 S. Wang, Y. Wang, S. L. Zhang, S.-Q. Zang and X. W. (David) Lou, *Advanced Materials*, 2019, **31**, 1903404.
12 12 Y. Sun, F. Wang, Y. Fu, C. Chen, X. Wang, Z. Xiao, Y. Liu, J. Xu, B. Li and L. Wang, *RSC Adv*, 2020, **10**, 812–817.
13 13 B. Poornaprakash, P. Puneetha, M. S. P. Reddy, S. Sangaraju, P. Rosaiah, B. A. Al-Asbahi, D.-Y. Lee and Y. L. Kim, *Journal of Materials Science: Materials in Electronics*, 2023, **34**, 1614.
14 14 A. Wu, L. Jing, J. Wang, Y. Qu, Y. Xie, B. Jiang, C. Tian and H. Fu, *Sci Rep*, 2015, **5**, 8858.
15 15 R. J. Vimal Michael, J. Theerthagiri, J. Madhavan, M. J. Umapathy and P. T. Manoharan, *RSC Adv*, 2015, **5**, 30175–30186.
16 16 H. Moon, M. S. Goh, M. Cha, U.-S. Kim, H. S. Whang, N. Son and M. Kang, *Appl Surf Sci*, 2022, **606**, 154787.

Journal of Materials Chemistry A Accepted Manuscript

This journal is © The Royal Society of Chemistry 20xx

Please do not adjust margins

View Article Online
DOI: 10.1039/D5TA03793J

Published on 28 August 2025. Downloaded by National Yang Ming Chiao Tung University on 9/8/2025 8:16:04 AM.

17 17 L. Tie, S. Yang, C. Yu, H. Chen, Y. Liu, S. Dong, J. Sun and J. Sun, *J Colloid Interface Sci*, 2019, **545**, 63–70.
18 18 J. Dong, W. Fang, W. Xia, Q. Lu and X. Zeng, *RSC Adv*, 2021, **11**, 21642–21650.
19 19 S. A. Thomas, N. Roy, W. Sharaf Saeed, A. Sreedhar and J. Cherusseri, *Int J Hydrogen Energy*, DOI:https://doi.org/10.1016/j.ijhydene.2023.06.302.
20 20 B. Poornaprakash, U. Chalapathi, P. T. Poojitha, S. V. P. Vattikuti and M. S. P. Reddy, *Journal of Materials Science: Materials in Electronics*, 2019, **30**, 9897–9902.
21 21 A. Es-Smairi, N. Fazouan, E. H. Atmani, M. Khuili and E. Maskar, *Applied Physics A*, 2021, **127**, 698.
22 22 V. Selvaraj, H. H. Mahboub, U. Ganapathi, S. K. Chandran, W. Al-Onazi, A. M. Al-Mohaimeed, T.-W. Chen, C. Faggio and B. Paulraj, *Environmental Science and Pollution Research*, 2022, **29**, 73528–73541.
23 23 N. Bansal, G. C. Mohanta and K. Singh, *Ceram Int*, 2017, **43**, 7193–7201.
24 24 X. Wang, X. Wang, J. Huang, S. Li, A. Meng and Z. Li, *Nat Commun*, 2021, **12**, 4112.
25 25 L. Bao, Y. Jia, X. Ren, X. Liu, C. Dai, S. Ali, M. Bououdina, Z. Lu and C. Zeng, *J Mater Sci Technol*, 2024, **199**, 75–85.
26 26 B. Xiao, T. Lv, T. Zhou, J. Zhao, X. Kuang, Y. Zhang, D. Wang, J. Zhang, Z. Zhu and Q. Liu, *ACS Catal*, 2023, **13**, 12904–12916.
27 27 M. Hafeez, B. A. Al-Asbahi, M. H. Hj Jumali, M. Yahaya, F. Inam, M. F. Bhopal and A. S. Bhatti, *Mater Sci Semicond Process*, 2020, **117**, 105193.
28 28 A. Kudo and M. Sekizawa, *Chemical Communications*, 2000, 1371–1372.
29 29 M. Kimi, L. Yuliati and M. Shamsuddin, *J Nanomater*, 2015, **2015**, 195024.
30 30 X. Shi, C. Dai, X. Wang, J. Hu, J. Zhang, L. Zheng, L. Mao, H. Zheng and M. Zhu, *Nat Commun*, 2022, **13**, 1287.
31 31 J. Zhang, Y. Wang, J. Zhang, Z. Lin, F. Huang and J. Yu, *ACS Appl Mater Interfaces*, 2013, **5**, 1031–1037.
32 32 M. M. Khan and K. O. Abdulwahab, *Mater Sci Semicond Process*, 2024, **181**, 108634.
33 33 V. S. Bhat, T. S. Tilakraj, M. K. Patil, V. Pujari, B. G. Mulimani and S. R. Inamdar, *J Mol Liq*, 2024, **396**, 123937.
34 34 I. Daskalakis, I. Vamvasakis, I. T. Papadas, S. Tsatsos, S. A. Choulis, S. Kennou and G. S. Armatas, *Inorg Chem Front*, 2020, **7**, 4687–4700.
35 35 L. Bao, Y. Dong, C. Dai, G. Xu, Y. Yang, X. liu, D. Ma, Y. Jia and C. Zeng, *Inorg Chem*, 2021, **60**, 15712–15723.
36 36 A. Azmand and H. Kafashan, *J Alloys Compd*, 2019, **779**, 301–313.
37 37 A. Azmand and H. Kafashan, *J Alloys Compd*, 2019, **779**, 301–313.
38 38 T. Takata, J. Jiang, Y. Sakata, M. Nakabayashi, N. Shibata, V. Nandal, K. Seki, T. Hisatomi and K. Domen, *Nature*, 2020, **581**, 411–414.
39 39 G. Jia, F. Sun, T. Zhou, Y. Wang, X. Cui, Z. Guo, F. Fan and J. C. Yu, *Nat Commun*, 2024, **15**, 4746.
40 40 A. Es-Smairi, N. Fazouan, E. H. Atmani, M. Khuili and E. Maskar, *Applied Physics A*, 2021, **127**, 698.
41 41 G. Kresse and J. Furthmüller, *Phys Rev B*, 1996, **54**, 11169–11186.
42 42 C. S. Pathak, D. D. Mishra, V. Agarwala and M. K. Mandal, *Ceram Int*, 2012, **38**, 5497–5500.
43 43 G. Zhu, S. Zhang, Z. Xu, J. Ma and X. Shen, *J Am Chem Soc*, 2011, **133**, 15605–15612.
44 44 X. Zhu, B. Cheng, J. Yu and W. Ho, *Appl Surf Sci*, 2016, **364**, 808–814.
45 45 J. N. Tiwari, S. Sultan, C. W. Myung, T. Yoon, N. Li, M. Ha, A. M. Harzandi, H. J. Park, D. Y. Kim, S. S. Chandrasekaran, W. G. Lee, V. Vij, H. Kang, T. J. Shin, H. S. Shin, G. Lee, Z. Lee and K. S. Kim, *Nat Energy*, 2018, **3**, 773–782.
46 46 C. Lee, W. Yang and R. G. Parr, *Phys Rev B*, 1988, **37**, 785–789.
47 47 J. P. Perdew, K. Burke and M. Ernzerhof, *Phys Rev Lett*, 1996, **77**, 3865–3868.
48 48 A. Tkatchenko, R. A. DiStasio, R. Car and M. Scheffler, *Phys Rev Lett*, 2012, **108**, 236402.
49 49 A. Kuzmin, M. Dile, K. Laganovska and A. Zolotarjovs, *Mater Chem Phys*, 2022, **290**, 126583.
50 50 Y. Chen and J. Chen, *Miner Eng*, 2010, **23**, 676–684.
51 51 X. Liu, Y. Zhang, S. Matsushima, T. Sugiyama, H. Hojo and H. Einaga, *ACS Appl Energy Mater*, 2022, **5**, 1849–1857.
52 52 Y. Zhang, J. Zhao, H. Wang, B. Xiao, W. Zhang, X. Zhao, T. Lv, M. Thangamuthu, J. Zhang, Y. Guo, J. Ma, L. Lin, J. Tang, R. Huang and Q. Liu, *Nat Commun*, 2022, **13**, 58.
53 53 X. Wu, H. Zhang, J. Dong, M. Qiu, J. Kong, Y. Zhang, Y. Li, G. Xu, J. Zhang and J. Ye, *Nano Energy*, 2018, **45**, 109–117.
54 54 Z.-H. Xue, D. Luan, H. Zhang and X. W. (David) Lou, *Joule*, 2022, **6**, 92–133.
55 55 Y. Fan, X. Hao, Y. Shao and Z. Jin, *Adv Sustain Syst*, 2024, **8**, 2300300.
56 56 H. Krishna Sadhanala, A. Maddegalla and K. K. Nanda, *New Journal of Chemistry*, 2017, **41**, 13742–13746.
57 57 A. Sanchez-Martinez, J. J. Marin-Perez, O. Ceballos-Sanchez, R. Ruelas, R. Ramírez-Bon, E. R. López-Mena and C. E. Pérez-García, *Journal of Materials Science: Materials in Electronics*, 2024, **35**, 993.
58 58 S. Benkoula, O. Sublemontier, M. Patanen, C. Nicolas, F. Sirotti, A. Naitabdi, F. Gaie-Levrel, E. Antonsson, D. Aureau, F.-X. Ouf, S.-I. Wada, A. Etcheberry, K. Ueda and C. Miron, *Sci Rep*, 2015, **5**, 15088.
59 59 G. Simões dos Reis, C. Mayandi Subramaniyam, A. D. Cárdenas, S. H. Larsson, M. Thyrel, U. Lassi and F. García-Alvarado, *ACS Omega*, 2022, **7**, 42570–42581.
60 60 C.-H. Kuan, Y.-C. Chen, S. Narra, C.-F. Chang, Y.-W. Tsai, J.-M. Lin, G.-R. Chen and E. W.-G. Diau, *ACS Energy Lett*, 2024, **9**, 2351–2357.
61 61 A. Abid, P. Rajamanickam and E. Wei-Guang Diau, *Chemical Engineering Journal*, 2023, **477**, 146755.
62 62 X. Wang, B. Liu, S. Ma, Y. Zhang, L. Wang, G. Zhu, W. Huang and S. Wang, *Nat Commun*, 2024, **15**, 2600.
63 63 M. Öztaş, M. Bedir, A. Necmeddin Yazici, E. Vural Kafadar and H. Toktamış, *Physica B Condens Matter*, 2006, **381**, 40–46.

Journal of Materials Chemistry A Accepted Manuscript

Please do not adjust margins

View Article Online
DOI: 10.1039/D5TA03793J

The data supporting this article have been included as part of the Supplementary Information.

Published on 28 August 2025. Downloaded by National Yang Ming Chiao Tung University on 9/8/2025 8:16:04 AM.

Journal of Materials Chemistry A Accepted Manuscript